
Compositional amortized inference for large-scale hierarchical Bayesian models

Jonas Arruda

Bonn Center for Mathematical Life Sciences,
& Life & Medical Sciences Institute
University of Bonn, Germany

Vikas Pandey

Center for Modeling, Simulation,
& Imaging in Medicine (CeMSIM)
Rensselaer Polytechnic Institute, NY, USA

Catherine Sherry

Molecular and Cellular Physiology
Albany Medical College, NY, USA

Margarida Barroso

Molecular and Cellular Physiology
Albany Medical College, NY, USA

Xavier Intes

Center for Modeling, Simulation,
& Imaging in Medicine (CeMSIM)
Rensselaer Polytechnic Institute, NY, USA

Jan Hasenauer

Bonn Center for Mathematical Life Sciences,
& Life & Medical Sciences Institute
University of Bonn, Germany

Stefan T. Radev

Center for Modeling, Simulation,
& Imaging in Medicine (CeMSIM)
Rensselaer Polytechnic Institute, NY, USA

Abstract

Amortized Bayesian inference (ABI) has emerged as a powerful simulation-based approach for estimating complex mechanistic models, offering fast posterior sampling via generative neural networks. However, extending ABI to hierarchical models, a cornerstone of modern Bayesian analysis, remains a major challenge due to the difficulty of scaling to large numbers of parameters. In this work, we build on compositional score matching (CSM), a divide-and-conquer strategy for Bayesian updating using diffusion models. To address existing stability issues of CSM, we propose adaptive solvers coupled with a novel, error-damping compositional estimator. Our proposed method remains stable even with hundreds of thousands of data points and parameters. We validate our approach on a controlled toy example, a high-dimensional spatial autoregressive model, and a real-world advanced microscopy biological application task involving over 750,000 parameters.

1 Introduction

Simulation-based inference [SBI; Diggle and Gratton, 1984, Cranmer et al., 2020] is entering a new era, leveraging deep learning advances to deliver markedly more efficient computational statistics. Within this framework, amortized Bayesian inference [Bürkner et al., 2023, ABI;] now scales Bayesian analysis to high-dimensional, mechanistic models, driving state-of-the-art discoveries in fields as diverse as astrophysics [Dax et al., 2025] and neuroscience [Tolley et al., 2024].

In retrospect, the core idea of ABI appears simple: train a conditional generative model on simulations from a parametric Bayesian model $p(\theta, \mathbf{Y})$ over parameters θ and (potentially high-dimensional) observables \mathbf{Y} . The network can then obtain independent samples from the posterior $p(\theta \mid \mathbf{Y})$ in a

fraction of the time required by gold-standard Markov chain Monte Carlo (MCMC) methods. And as simple benchmarking suites have already received extensive attention [Lueckmann et al., 2021], recent research increasingly turns to a more pressing challenge in Bayesian inference: affording amortized inference for *hierarchical*, *mixed-effects*, or *multilevel models* [Rodrigues et al., 2021, Heinrich et al., 2023, Arruda et al., 2024, Habermann et al., 2024].

In many application domains, Hierarchical models (HMs) are the default choice in Bayesian data analysis [Gelman et al., 2013, McElreath, 2018]. Their nested structure, however, strains inference algorithms: standard MCMC rarely scales to large data sets [Blei et al., 2017, Margossian and Saul, 2023], and amortized Bayesian inference (ABI) faces both network-design and simulation-efficiency hurdles. Crucially, direct ABI approaches for estimating HMs require exhaustive simulations for each training sample (cf. Figure 1, left). This renders existing ABI approaches impractical for many real-world hierarchical models, particularly those involving large datasets or expensive simulators.

To overcome this bottleneck, we build on *compositional score matching* (CSM), a divide-and-conquer strategy originally introduced for Bayesian updating across exchangeable data points [Geffner et al., 2023], and recently adapted to complete pooling [Linhart et al., 2024] and time series models [Gloeckler et al., 2024b]. By partitioning hierarchical estimation into multiple non-hierarchical problems, our approach enables efficient training for amortizing HMs (cf. Figure 1, right). Moreover, it affords modern score-based diffusion models [Song and Ermon, 2019, Song et al., 2020] that have already shown considerable potential in SBI [Sharrock et al., 2024] and ABI [Gloeckler et al., 2024a].

Despite the conceptual appeal of CSM, we observe that current aggregation methods fail even for simple, non-hierarchical models as the number of observations grows. Here, we show that these instabilities are due to compounding approximation errors and introduce a new compositional estimator that remains stable even in hierarchical models with more than 250,000 groups and 750,000 parameters. Concretely, we develop and showcase

1. A new divide-and-conquer method for estimating large hierarchical Bayesian models with score-based diffusion samplers;
2. A stable reformulation of compositional score matching with stochastic differential equations (SDEs) using adaptive solvers;
3. An error-damping mini-batch estimator that enables efficient scaling as the number of groups J becomes very large (e.g., hundreds of thousands of individual time series).

2 Background and related work

Hierarchical Bayesian models Hierarchical Bayesian models are the default choice to model dependencies in nested data, where observations are organized into clusters or levels [Gelman et al., 2013]. From a Bayesian perspective, any parametric data model $p(\mathbf{Y} \mid \boldsymbol{\theta})$ can incorporate multilevel structure via a hierarchical prior. For instance, a two-level model defines two generative stages

$$\mathbf{Y}_j \sim p(\mathbf{Y}_j \mid \boldsymbol{\theta}_j, \boldsymbol{\eta}), \quad \boldsymbol{\theta}_j \sim p(\boldsymbol{\theta} \mid \boldsymbol{\eta}), \quad \boldsymbol{\eta} \sim p(\boldsymbol{\eta}), \quad (1)$$

via a *hyperprior* $p(\boldsymbol{\eta})$ capturing global variation and a *conditional prior* $p(\boldsymbol{\theta} \mid \boldsymbol{\eta})$ capturing local variation. The task of Bayesian estimation is to estimate the full joint posterior over local and global parameters:

$$p(\boldsymbol{\eta}, \boldsymbol{\theta}_1, \dots, \boldsymbol{\theta}_J \mid \mathbf{Y}_1, \dots, \mathbf{Y}_J) \propto p(\boldsymbol{\eta}) \prod_{j=1}^J p(\mathbf{Y}_j \mid \boldsymbol{\theta}_j) p(\boldsymbol{\theta}_j \mid \boldsymbol{\eta}), \quad (2)$$

where J denotes the number of groups and the data model generally factorizes over N_j observations within group j as $p(\mathbf{Y}_j \mid \boldsymbol{\theta}_j) = \prod_{n=1}^{N_j} p(\mathbf{y}_{j,n} \mid \boldsymbol{\theta}_j, \mathbf{y}_{j,1:n-1})$.

The gold-standard approach for estimating hierarchical models are Markov chain Monte Carlo (MCMC) methods [Gelman et al., 2020]. While MCMC methods offer strong theoretical guarantees, they are typically too slow for real-time or big data applications. Moreover, MCMC cannot be trivially applied to simulation-based models [Sisson and Fan, 2011], hence the appeal of amortized inference.

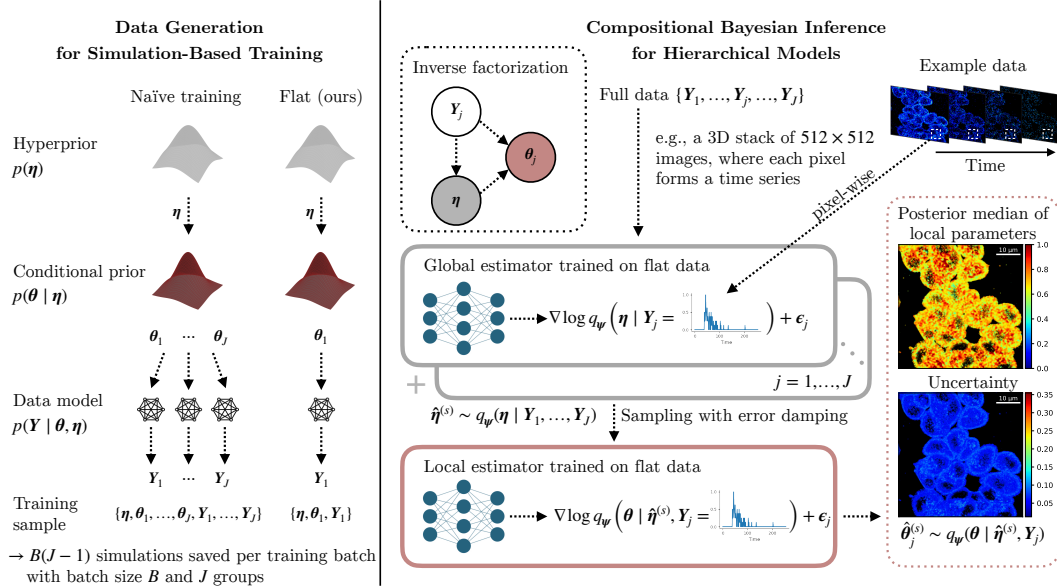


Figure 1: *Compositional inference for hierarchical Bayesian models.* Overview of our training procedure (left) and inference stages (right) for amortized hierarchical Bayesian modeling. Amortized posterior sampling uses our error-damping compositional score estimator to achieve rapid inference on very high-dimensional hierarchical problems.

Amortized Bayesian inference (ABI) In amortized Bayesian inference (ABI), a generative network seeks to learn a global posterior functional, $\mathbf{Y} \mapsto q(\boldsymbol{\theta} \mid \mathbf{Y})$. Typically, the network minimizes a strictly proper scoring rule \mathcal{S} [Gneiting et al., 2007] in expectation over the joint model $p(\boldsymbol{\theta}, \mathbf{Y})$:

$$\min_q \left\{ \mathbb{E}_{p(\boldsymbol{\theta}, \mathbf{Y})} [\mathcal{S}(q(\cdot \mid \mathbf{Y}), \boldsymbol{\theta})] \approx \frac{1}{B} \sum_{b=1}^B \mathcal{S}(q(\cdot \mid \mathbf{Y}^{(b)}), \boldsymbol{\theta}^{(b)}) \right\}. \quad (3)$$

Using a universal density estimator for q , such as coupling flows [Draxler et al., 2024], ensures that Eq. 3 can, in principle, converge to the correct target for large simulation budgets $B \rightarrow \infty$. Since \mathbf{Y} is typically high-dimensional, a summary network $h(\mathbf{Y})$ can be jointly trained to learn data embeddings on the fly [Radev et al., 2020] or implicitly incorporated into the architecture of q [Gloeckler et al., 2024a]. Crucially, q repays users with zero-shot sampling for any new observation $\mathbf{Y}^{(\text{new})}$ compatible with $p(\boldsymbol{\theta}, \mathbf{Y})$, making ABI an attractive avenue for efficiently fitting complex hierarchical models.

ABI for hierarchical models Previous work has already ported the basic idea of ABI to hierarchical settings [Habermann et al., 2024, Arruda et al., 2024, Heinrich et al., 2023, Rodrigues et al., 2021]. These works leverage the inverse factorization of Eq. 1 in different ways to design hierarchical neural networks with inductive biases that capture the probabilistic symmetries (e.g., permutation invariance for exchangeable groups) of HMs. However, these approaches either approximate only parts of the joint posterior (Eq. 1) or scale poorly even when the number of groups J becomes moderately large.

Scalability issues arise since the expectation in Eq. 3 now runs over $p(\boldsymbol{\eta}, \boldsymbol{\theta}_1, \dots, \boldsymbol{\theta}_J, \mathbf{Y}_1, \dots, \mathbf{Y}_J)$, necessitating the simulation of a data set of data sets $\{\mathbf{Y}_1, \dots, \mathbf{Y}_J\}$ for each batch instance (cf. Figure 1, left): even for $J \approx 1000$, a single training batch requires tens of thousands of simulations, exceeding typical simulation budgets for non-trivial models quickly. Similar-sized problems can also become practically infeasible for established MCMC samplers [e.g., NUTS Hoffman et al., 2014] even for models with closed-form likelihoods (see **Experiment 2**).

Inspired by Geffner et al. [2023], Linhart et al. [2024], Gloeckler et al. [2024b], we address these efficiency issues in a “divide-and-conquer” manner via compositional score matching (CSM; cf. Figure 1, right). Along the way, we introduce several key improvements to CSM in terms of stability and scalability. To the best of our knowledge, we provide the first simulation-based method capable of handling large-scale hierarchical Bayesian models with or without explicit likelihoods.

Table 1: Convergence of sampling methods for Gaussian toy example (**Experiment 1**) with a maximum budget of 10,000 compositional sampling steps (✓ – converges, ✗ – fails).

Method	$N=10$	$N=100$	$N=10k$	$N=100k$
Annealed Langevin sampler	✓	✗	✗	✗
Euler-Maruyama sampler	✓	✗	✗	✗
Probability ODE sampler	✓	✓	✗	✗
Adaptive second-order sampler	✓	✓	✗	✗
Any sampler with damping (ours)	✓	✓	✓	✓
Any sampler with schedule adjustment (ours)	✓	✓	✓	✓

Score matching Score-based modeling [Song and Ermon, 2019] and diffusion models [Ho et al., 2020] provide a powerful framework for generative modeling by learning to reverse a noise-adding process. In a non-hierarchical setting, diffusion models define a forward process that gradually corrupts a sample θ into pure noise, at each time step $t \in [0, 1]$ typically taking the form

$$\theta_t = \alpha_t \theta + \sigma_t \epsilon \quad \text{with} \quad \epsilon \sim \mathcal{N}(0, \mathbf{I}).$$

The factors α_t and σ_t are time-dependent functions that satisfy $\alpha_t^2 + \sigma_t^2 = 1$ for variance-preserving processes. These functions are often parameterized in terms of the log signal-to-noise ratio $\lambda_t = \log(\alpha_t^2 / \sigma_t^2)$, known as the *noise schedule* of the forward process [Kingma and Gao, 2023].

The conditional denoising score matching loss can be expressed in terms of an unconditional score, as shown by Li et al. [2024], and further reformulated as an ϵ -prediction objective following Kingma and Gao [2023]:

$$\min_{\psi} \mathbb{E}_{p(\theta, \mathbf{Y})} \mathbb{E}_{t \sim \mathcal{U}(0,1), \epsilon \sim \mathcal{N}(0, \mathbf{I})} [w_t \|\epsilon - \hat{\epsilon}_{\psi}(\theta_t, \mathbf{Y}, \lambda_t)\|_2^2], \quad (4)$$

which assumes the equivalent score parameterization $\hat{\epsilon} = -s_{\psi}(\theta_t, \mathbf{Y}, \lambda_t)\sigma_t$. The weighting function $w_t > 0$, often chosen to match the noise schedule λ_t (see Kingma and Gao [2023] for a detailed review of different weighting functions and noise schedules), is instantiated here as the likelihood weighting proposed by Song et al. [2021]. The forward and backward diffusion process can be specified as a stochastic differential equation [SDE; Song et al., 2020], which enables posterior sampling using state-of-the-art SDE solvers (more details in Appendix A.1). Moreover, it has neither been used for hierarchical modeling nor explored for compositional score matching in prior work Geffner et al. [2023], Linhart et al. [2024], Gloeckler et al. [2024b], as discussed next.

3 Method

3.1 Compositional score matching

A major challenge in Bayesian inference arises when dealing with varying and potentially large numbers of observations, especially in hierarchical models. To address this for non-hierarchical models, Geffner et al. [2023] introduced *compositional score matching* (CSM) that enables the combination of multiple conditionally independent score estimates into a global posterior approximation.

Suppose we have J exchangeable groups $\{\mathbf{Y}_j\}_{j=1}^J$, then we can divide the groups in $k = \lfloor J/m \rfloor$ subsets of size m , where we denote the group in subset i with an additional index l_i . Then, the compositional posterior can be written as $p(\theta \mid \{\mathbf{Y}_j\}_{j=1}^J) = p(\theta)^{1-k} \prod_{i=1}^k p(\theta \mid \{\mathbf{Y}_{l_i}\}_{l_i=1}^m)$ using Bayes’ rule twice. Here, m determines the number of simulations we need to perform to generate one sample for training as we condition the score on multiple groups. The larger m gets, the more simulations for training are needed, but this might reduce approximation error of the score. As a bridging density between the latent diffusion prior, a spherical Gaussian $p_{t=1}(\theta) = \mathcal{N}(\mathbf{0}, \frac{1}{k}\mathbf{I})$, and the posterior $p_{t=0}(\theta \mid \{\mathbf{Y}_j\}_{j=1}^J)$, Geffner et al. [2023] choose a linear interpolation between the prior and the individual posterior scores

$$\nabla_{\theta} \log p_t(\theta \mid \{\mathbf{Y}_j\}_{j=1}^J) = (1-k)(1-t) \nabla_{\theta} \log p(\theta) + \sum_{i=1}^k \nabla_{\theta} \log p_t(\theta \mid \{\mathbf{Y}_{l_i}\}_{l_i=1}^m). \quad (5)$$

This allows us to train a single score network on samples $(\theta_i, \{\mathbf{Y}_{l_i}\}_{l_i=1}^m) \sim p(\theta)p(\{\mathbf{Y}_{l_i}\}_{l_i=1}^m | \theta)$. After training, we can perform inference by sampling from the latent prior $p_{t=1}(\theta) = \mathcal{N}(\mathbf{0}, \frac{1}{k}\mathbf{I})$ and then using the compositional score to sample from the posterior.

Geffner et al. [2023] employ a Langevin sampling scheme to invert the diffusion process for posterior inference, which needs many score evaluations for accurate inference [Jolicœur-Martineau et al., 2021] and is sensitive to the choices of step-size at each sampling iteration [Linhart et al., 2024]. In contrast, Linhart et al. [2024] propose a second order approximation of the backward diffusion kernels to bypass the need for Langevin dynamics, however introducing the need to approximate potentially large covariance matrices, limiting their experiments to only 100 observations.

In the remainder, we demonstrate that it is possible to leverage the SDE formulation by using the compositional score in the reverse SDE (see Appendix A.1) to sample from the posterior distribution. This allows us to use more efficient numerical solvers. However, regardless of the number of conditioning groups k , increasing the number of score terms leads to error compounding, resulting in unstable dynamics and divergent samples (see Figure 6 in Appendix). Even higher-order solvers require extremely small step sizes, constraining their practicality (cf. Table 1). To address this, we introduce an error-damping, unbiased mini-batch estimator and demonstrate its scalability.

3.2 Compositional hierarchical score matching

In this study, we propose to approximate the posterior distributions at various levels of a hierarchical model using score matching. Each level is associated with its own neural estimator, responsible for modeling the corresponding posterior distribution. This is similar to the framework introduced by Habermann et al. [2024] and Heinrich et al. [2023] but avoids the need for hierarchical embeddings.

At each level, the posterior is modeled via a conditional score function. At higher levels of the hierarchy, we leverage the compositional score framework, enabling training of the global model on single groups. For example, in a two level model, we have

$$s_{\psi_{\text{local}}}(\theta_j, \boldsymbol{\eta}, \mathbf{Y}_j, \lambda_t) \approx \nabla_{\theta_j} \log p_t(\theta_j | \boldsymbol{\eta}, \mathbf{Y}_j), \quad s_{\psi_{\text{global}}}(\boldsymbol{\eta}, \mathbf{Y}_j, \lambda_t) \approx \nabla_{\boldsymbol{\eta}} \log p_t(\boldsymbol{\eta} | \mathbf{Y}_j). \quad (6)$$

For each group, we may learn a shared summary representation $\mathbf{h}_j = h(\mathbf{Y}_j)$ via a summary network h . Either the raw data \mathbf{Y}_j or its summary \mathbf{h}_j is then used as input to both the global and local score-based models. The design of the summary h should be adapted to the specific data modality (e.g., recurrent networks or transformers for time series, etc). When conditioning on multiple groups, we utilize exchangeability via a second summary network (e.g., a Deep Set model [Zaheer et al., 2017]), which aggregates the individual summaries into a permutation-invariant global summary.

Both the global and local score networks can be trained jointly via denoising score matching objectives, allowing the system to share representations and learn in a coherent hierarchical fashion:

$$\min_{\psi} \mathbb{E}_{p(\theta, \boldsymbol{\eta}, \mathbf{Y})} \mathbb{E}_{t \sim \mathcal{U}(0,1)} w_t \left[\|\epsilon + s_{\psi_{\text{local}}}(\theta_t, \boldsymbol{\eta}, \mathbf{Y}, \lambda_t) \sigma_t\|_2^2 + \|\epsilon + s_{\psi_{\text{global}}}(\boldsymbol{\eta}_t, \mathbf{Y}, \lambda_t) \sigma_t\|_2^2 \right], \quad (7)$$

with $\boldsymbol{\eta}_t = \alpha_t \boldsymbol{\eta} + \sigma_t \epsilon$ and $\theta_t = \alpha_t \theta + \sigma_t \epsilon$, where $\epsilon \sim \mathcal{N}(0, \mathbf{I})$. Having trained a global and a local model, we can sample from the joint posterior by

$$\boldsymbol{\eta}^{(s)} \sim q_{\psi_{\text{global}}}(\boldsymbol{\eta} | \{\mathbf{Y}_j\}_{j=1}^J), \quad \theta_j^{(s)} \sim q_{\psi_{\text{local}}}(\theta | \boldsymbol{\eta}^{(s)}, \mathbf{Y}_j), \quad (8)$$

where we leverage the compositional score for the global parameters and then sample the local ones.

3.3 Scalable compositional score matching

We propose using the SDE formulation to perform compositional inference with adaptive solvers—avoiding the need for annealed Langevin sampling, which requires many steps per noise level and becomes prohibitively expensive when error correction is needed. This allows us to leverage an adaptive solver that automatically adjusts the step size during integration, which is especially beneficial for large values of J , where the need for finer granularity (i.e., smaller step sizes) increases and manual tuning becomes infeasible [Jolicœur-Martineau et al., 2021].

However, two main challenges remain in scaling the compositional approach to large datasets: 1) the bridging densities introduced by Geffner et al. [2023] become unstable as J increases (see Table 1) and 2) the memory requirements grow substantially when accumulating scores over the full data set.

Flexible error-dampening bridging densities The stability of the bridge density might be improved by introducing a damping factor of the accumulated score. Yet, naively applying a dampening factor to the compositional score to prevent it from diverging would bias the posterior sample. Instead, to mitigate instability at large J , we introduce a more flexible class of error-dampening bridging densities:

$$p_t(\boldsymbol{\theta} \mid \{\mathbf{Y}_j\}_{j=1}^J) \propto (p(\boldsymbol{\theta})^{1-J})^{(1-t)d(t)} \prod_{j=1}^J p_t(\boldsymbol{\theta} \mid \mathbf{Y}_j)^{d(t)}, \quad (9)$$

where $d(0) = d_0 = 1$ and $d(1) = d_1 \leq 1$ and latent diffusion prior $p_{t=1}(\boldsymbol{\theta}) = \mathcal{N}(0, \frac{1}{nd_1}\mathbf{I})$.

The key idea is to define a monotonic function $d(t)$ that moderates the accumulation of score contributions throughout the diffusion trajectory. In high-noise regimes, we reduce the influence of the individual terms to prevent the score from diverging, while for $t \rightarrow 0$, we allow their contributions to accumulate, recovering the true posterior. This construction is motivated by the observation that adaptive solvers require smaller steps in high-noise regimes to avoid numerical instability (see Appendix Figure 6). As damping schedule, we use an exponential decay $d(t) = d_0 \cdot \exp(-\ln(d_0/d_1) \cdot t)$ with $d_0 = 1$ and a hyperparameter d_1 that can be tuned during inference.

Mini-batch estimation for memory efficiency To address memory constraints in large-data scenarios, we introduce a mini-batch estimator for the compositional score:

$$\hat{s}_\psi(\boldsymbol{\theta}, \{\mathbf{Y}_j\}_{j=1}^J, \lambda_t) = (1-J)(1-t)\nabla_{\boldsymbol{\theta}} \log p(\boldsymbol{\theta}) + \frac{J}{M} \sum_{i=1}^M s_\psi(\boldsymbol{\theta}, \mathbf{Y}_{j_i}, \lambda_t), \quad (10)$$

where $j_i \sim \mathcal{U}\{1, \dots, J\}$ and M is the mini-batch size.

Proposition 1. *The mini-batch estimator in (10) is an unbiased estimate of the compositional score.*

For a short proof, see Appendix A.2. Combining this estimator with the dampening function yields our final form:

$$\hat{s}_\psi^d(\boldsymbol{\theta}, \{\mathbf{Y}_j\}_{j=1}^J, \lambda_t) = d(t) \cdot \left((1-J)(1-t)\nabla_{\boldsymbol{\theta}} \log p(\boldsymbol{\theta}) + \frac{J}{M} \sum_{i=1}^M s_\psi(\boldsymbol{\theta}, \mathbf{Y}_{j_i}, \lambda_t) \right). \quad (11)$$

This *error-damping mini-batch estimator* scales well with dataset size and maintains stability across the reverse-time diffusion process.

Noise schedule adjustment for sampling We propose using different noise schedules for training and inference. During inference, spending less time in the high-noise region improves stability and allows for larger step sizes, which is particularly important in the large- J regime. In the case of the cosine schedule $\lambda(t) = -2 \cdot \log(\tan(\pi t/2)) + 2s$ proposed by Nichol and Dhariwal [2021], this can be easily achieved by increasing the shift parameter s , which effectively compresses the high-noise segment of the schedule. As discussed by Karras et al. [2022] and Kingma and Gao [2023], the combination of the noise schedule and the weighting function in the denoising score matching objective plays a role akin to importance sampling.

4 Experiments

To systematically evaluate the proposed methods, we consider three case studies.

- **Gaussian toy example:** An analytically tractable Gaussian model with up to 100,000 synthetic data points, used to assess the accuracy and breakdown point of compositional score estimation.
- **Hierarchical time series model:** A grid of AR(1) processes with shared global and local parameters, used to evaluate joint inference performance against MCMC.
- **Real-world application:** Time-resolved Bayesian decay analysis in Fluorescence Lifetime Imaging (FLI), used to demonstrate scalability to high-dimensional real data.

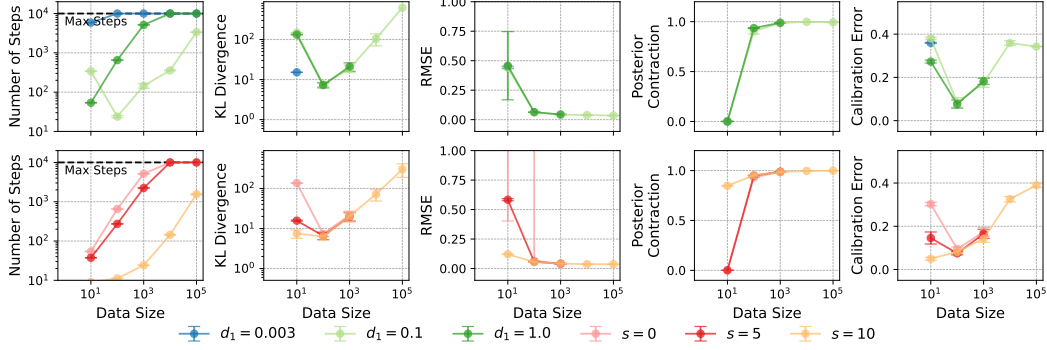


Figure 2: *Evaluation of the error-damping estimator for the toy example.* Different evaluation metrics are shown for different data set sizes and damping factors d_1 or cosine sifts s . The mini-batch size was set to 10% of the data set size and for each step 10 runs were performed. The median and median absolute deviation is reported besides for those step 10 runs where none converged.

For the two synthetic examples, we assess convergence across varying data sizes by recording the number of sampling iterations of the adaptive sampler. In the Gaussian toy example, we can calculate the KL divergence between the compositional and the true posteriors, relative mean squared error (RMSE) normalized by the known variance, posterior contraction, and calibration error (Appendix A.3). For the hierarchical models, we compute these metrics separately at both the global and the local level. Appendix A.4 provides further details about the architecture.

4.1 Experiment 1: scaling and stabilizing CSM with error-damping mini-batch estimation

This first experiment serves both as a sanity check and as a demonstration of the stabilizing effects of our error-damping estimator, highlighting the accuracy and scalability of compositional score matching in a controlled setting. We consider a Gaussian model of dimension $D=10$ with conditionally independent groups and a global latent variable (see Appendix A.5). Since the posterior is analytically tractable, it enables precise measurement of accuracy and convergence. We scale the number of observations up to 100,000 to test the effect of dataset size on error accumulation of the individual scores. Below, we summarize our results and provide practical recommendations.

Damping factor We find that the optimal damping factor d_1 depends on the number of composed groups: larger datasets require smaller damping factors for convergence (Figure 2). However, overly small factors can prevent posterior contraction, worsen calibration, and even hinder convergence. With an initial factor of 0.003, we successfully compose 100,000 scores. At this scale, the analytical posterior becomes nearly a point estimate, so even slight deviations in our estimate can significantly increase the KL-divergence, but the RMSE remain negligible. The damping factor is a tunable hyperparameter, and a value on the order of $1/n$ often serves as a good starting point.

Mini-batching Our mini-batch estimator reduces computational cost per sampling step but does not resolve instability due to score error accumulation, which prevents convergence beyond 1000 groups (see Appendix Figure 7). Using smaller batches instead of the full dataset lowers both the KL-divergence and posterior calibration error, albeit with a slight increase in RMSE. We attribute this to a smoothing effect on accumulated score errors. In practice, we recommend using mini-batches of about 10% of the data to balance robustness and computational demands.

Noise schedule shifting Adjusting the noise schedule improves stability and mitigates error accumulation (Appendix Figure 7). A large shift of $s=10$ enables scaling to 100,000 groups and improves KL-divergence, RMSE, and calibration error. As expected, both KL-divergence and calibration degrade with larger datasets due to increased error accumulation, but the shifted schedule helps to mitigate this effect. Moreover, linear or EDM sampling schedules appear suboptimal for compositional score matching, failing to converge even on smaller datasets (see Appendix Figure 8).

Number of conditions Computing joint scores based on groups of 100 groups allows inference on up to 100,000 groups (Appendix Figure 7). However, increasing the number of conditioning groups

Table 2: Benchmarking against NUTS (gold-standard MCMC) for the hierarchical AR(1) model.

Method	RMSE Global	Contraction global	RMSE Local	Contraction local
NUTS (4x4)	0.08 (0.05)	0.95 (0.04)	0.1 (0.01)	0.98 (0.00)
Ours (4x4)	0.09 (0.05)	0.97 (0.0)	0.14 (0.01)	0.95 (0.01)
NUTS (32x32)	0.02 (0.01)	1.0 (0.0)	0.09 (0.01)	0.99 (0.0)
Ours (32x32)	0.08 (0.03)	1.0 (0.0)	0.15 (0.01)	0.97 (0.01)
NUTS (128x128)	N/A	N/A	N/A	N/A
Ours (128x128)	0.09 (0.05)	1.0 (0.01)	0.13 (0.01)	0.97 (0.01)

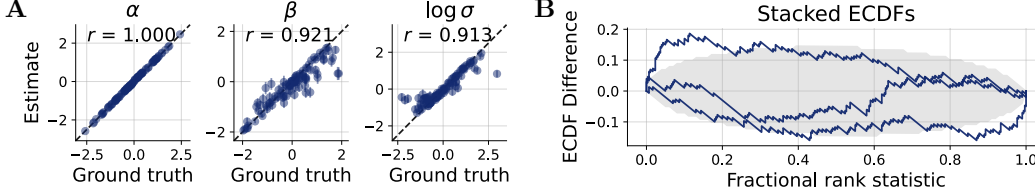


Figure 3: *Assessing inference for high-resolution grids (128x128).* **A** Global parameter recovery across datasets, showing the posterior median and median absolute deviation. **B** Posterior calibration plot for the global parameters, using the graphical diagnostic method from Säilynoja et al. [2022].

does not necessarily lead to better posterior contraction or lower RMSE. Notably, the number of conditions has to be chosen before training, and conditioning on more groups requires additional simulations, since each training sample incorporates multiple groups. Further, we find that the latter demand better network capacity, otherwise, RMSE deteriorates. In practice, using a small number of conditions can yield performance gains without incurring major training cost.

In summary, our experiment with the analytically tractable Gaussian toy example demonstrates that the error-damping mini-batch estimator affords scalable compositional inference for up to 100,000 groups. While mini-batching alone is insufficient to ensure convergence, combining it with damping and noise schedule shifting reduces score accumulation errors and computational cost.

4.2 Experiment 2: scaling hierarchical Bayesian inference

Our second experiment evaluates whether compositional score matching can accurately infer both global and local parameters for a non-trivial hierarchical model. We simulate a grid of local AR(1) processes with a shared global drift and local variation parameters (see Appendix A.6). We increase the grid size from 4x4 to 128x128 to test the scalability of the method, resulting in up to 16,384 local latent vectors.

For this grid of AR(1) processes direct comparison to NUTS [as implemented in Stan Carpenter et al., 2017] is possible, which is widely regarded as a gold standard for Bayesian inference and provides the most reliable benchmark for evaluating how well our method captures the correct shrinkage in the local parameters. Thus, we compare our approach with Stan on grids up to a resolution of 32x32. At this resolution, posterior sampling with Stan for 100 datasets takes a similar amount of time as training one score-based model and performing amortized inference across the same datasets.

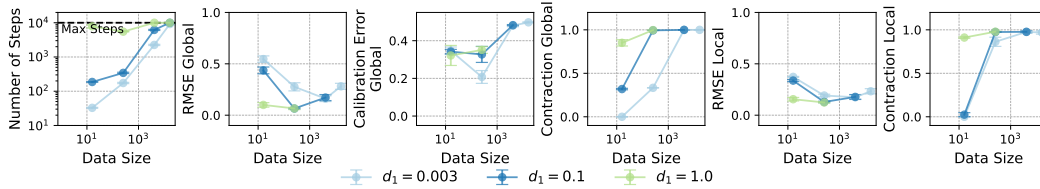


Figure 4: *Evaluation of the error-damping estimator for the hierarchical AR(1) model.* Different evaluation metrics are shown for different data set sizes and damping factors d_1 .

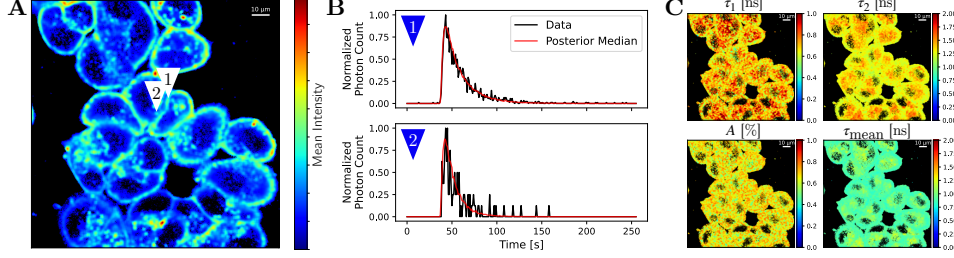


Figure 5: *Inference for fluorescence lifetime imaging.* **A** Mean intensity across time for each pixel, representing the fluorescence data. **B** Time series data and fitted posterior median for representative pixels. **C** Spatial map of the fitted local posteriors (medians) across the full image and mean lifetime.

Our experiments with the hierarchical model on the damping factor support the earlier findings: tuning the damping function is essential to balance posterior contraction and estimation error (Figure 4), however a too large cosine shift might hinder calibration. Moreover, *we find that neither the damping factor nor the cosine shift alone is sufficient to ensure convergence on high-resolution grids (e.g., 128×128), but their combination stabilizes inference (Figure 3-4).* However, for these large-scale settings, achieving well-calibrated posteriors often comes at the cost of reduced accuracy in parameter recovery. This difficulty arises due to the strong contraction of the posterior in hierarchical models. As a result, calibration becomes especially challenging in the high-resolution regime.

We observe that our method yields results comparable to NUTS at both the global and local parameter levels (Table 2; showing mean and standard deviation over parameters), with a bit higher RMSE on the local level. Crucially, our method scales effortlessly to significantly larger grid sizes, such as 128×128 (Figure 3). In contrast, Stan becomes computationally infeasible at this scale: inference for 100 datasets on such grids would require approximately 16 hours, whereas our approach completes inference within a few minutes using the learned score model.

In summary, our experiment with the grid of AR(1) processes shows that compositional score matching, when combined with damping and noise schedule shifting, enables accurate and scalable inference in hierarchical models with thousands of groups. Our method performs comparably to MCMC on small grids and remains stable on large grids where MCMC becomes computationally infeasible. While strong posterior contraction introduces challenges for calibration at scale, the proposed approach offers a practical and efficient approach for amortized hierarchical inference.

4.3 Experiment 3: application to fluorescence lifetime imaging (FLI)

Fluorescence lifetime imaging (FLI) is an important tool in pre-clinical cancer imaging, particularly for *in vivo* drug-target analysis [Verma et al., 2025]. However, FLI remains challenging due to its reliance on time-resolved acquisition at sub-nanosecond resolution, computationally intensive pixel-wise curve fitting, and noisy decay profiles caused by low quantum yield dyes, resulting in high uncertainty in lifetime estimates [Yuan et al., 2024, Trinh and Esposito, 2021]. A Bayesian approach has been explored in prior work [Wang et al., 2019, Rowley et al., 2016], but to our knowledge, this is the first application of a fully hierarchical Bayesian model to FLI data.

We analyze time-resolved fluorescence decay data from FLI (Figure 5A). Therefore, each pixel in the measured 512×512 images is modeled using a bi-exponential decay with local decay rates and mixture weights (Figure 5B), resulting in a hierarchical inference problem with over 250,000 groups. Unlike amortized methods that require full-image simulations to generalize across spatial structures, our approach trains on pixel-wise simulations, *requiring only the equivalent of 350 images*.

To assess the performance of the standard non-hierarchical approach and our proposed method, we first consider synthetic FLI data. We found that per-pixel maximum likelihood estimation (MLE) fails to recover the ground truth due to photon-limited noise. In contrast, our hierarchical approach accurately captures both global and local structures (Appendix 4.3). Nevertheless, estimating global variances remains challenging under very high noise conditions.

Encouraged by these results, we applied the method to real FLI data (details in Appendix 4.3). Using the trained score-based hierarchical model, we efficiently and reliably fit over 750,000 local parameters (Figure 5C). The inferred mean lifetime closely matches that of a standard MLE fit

(Appendix Figure 13), which is commonly recovered by conventional methods [Torrado et al., 2024]. Moreover, the model achieves excellent fits across the full image, as illustrated by representative decay curves and their posterior median reconstructions (Figure 5B).

In summary, this experiment demonstrates the scalability and practical utility of our approach for real-world data, enabling stable posterior estimates where traditional methods struggle with noise or high dimensionality.

5 Conclusion

HM are of outstanding importance, but their inference remains challenging. Here, we demonstrated that compositional score matching (CSM) provides a scalable and flexible framework for estimating non-trivial hierarchical Bayesian models. Moreover, we introduced an error-damping mini-batch estimator that resolves the inherent instability of CSM up to hundreds of thousands of data points. As a notable limitation, we observed that posterior calibration becomes difficult at scale, particularly under extreme contraction. While our dampening strategy reduces instability, achieving good calibration across all levels is an open problem. Future work could further explore temporal aggregation [Gloeckler et al., 2024b], systematically test the trade-off introduced by different dampening schedules, refine mini-batch selection using informativeness criteria [Peng et al., 2019], and generalize to more than two levels.

Acknowledgments

This work was supported by the German Federal Ministry of Education and Research (BMBF) (EMUNE/031L0293C), the European Union via the ERC grant INTEGRATE, grant agreement number 101126146, and under Germany’s Excellence Strategy by the Deutsche Forschungsgemeinschaft (DFG, German Research Foundation) (EXC 2047—390685813, EXC 2151—390873048), the University of Bonn via the Schlegel Professorship of J.H., and the National Science Foundation under Grant No. 2448380. J.A. thanks the Global Math Exchange Program of the Hausdorff Center for Mathematics for their financial support. We also thank Niels Bracher for his helpful insights on diffusion models. Views and opinions expressed are however those of the authors only and do not necessarily reflect those of the funding agencies.

Author CRediT

J.A.: Conceptualization, Methodology, Software, Formal analysis, Validation, Visualization, Funding acquisition, Writing – original draft, Writing – review & editing. V.P.: Data curation, Software, Writing – review & editing. C.S.: Investigation, Data curation, Writing – review & editing. M.B.: Supervision, Investigation, Data curation, Writing – review & editing. X.I.: Supervision, Project administration, Resources, Writing – review & editing. J.H.: Supervision, Project administration, Funding acquisition, Writing – review & editing. S.T.R.: Conceptualization, Methodology, Supervision, Resources, Funding acquisition, Writing – original draft, Writing – review & editing.

References

- J. Arruda, Y. Schälte, C. Peiter, O. Teplytska, U. Jaehde, and J. Hasenauer. An amortized approach to non-linear mixed-effects modeling based on neural posterior estimation. In *International Conference on Machine Learning*, pages 1865–1901. PMLR, 2024.
- M. Betancourt and M. Girolami. Hamiltonian monte carlo for hierarchical models. *Current trends in Bayesian methodology with applications*, 79(30):2–4, 2015.
- D. M. Blei, A. Kucukelbir, and J. D. McAuliffe. Variational inference: A review for statisticians. *Journal of the American Statistical Association*, 112(518):859–877, Apr. 2017. ISSN 0162-1459. doi: 10.1080/01621459.2017.1285773.
- P.-C. Bürkner, M. Scholz, and S. T. Radev. Some models are useful, but how do we know which ones? towards a unified bayesian model taxonomy. *Statistic Surveys*, 17:216–310, 2023.

- B. Carpenter, A. Gelman, M. D. Hoffman, D. Lee, B. Goodrich, M. Betancourt, M. Brubaker, J. Guo, P. Li, and A. Riddell. Stan: A probabilistic programming language. *Journal of statistical software*, 76:1–32, 2017.
- K. Cranmer, J. Brehmer, and G. Louppe. The frontier of simulation-based inference. *Proceedings of the National Academy of Sciences*, 117(48):30055–30062, 2020.
- M. Dax, S. R. Green, J. Gair, N. Gupte, M. Pürner, V. Raymond, J. Wildberger, J. H. Macke, A. Buonanno, and B. Schölkopf. Real-time inference for binary neutron star mergers using machine learning. *Nature*, 639(8053):49–53, 2025.
- P. J. Diggle and R. J. Gratton. Monte carlo methods of inference for implicit statistical models. *Journal of the Royal Statistical Society Series B: Statistical Methodology*, 46(2):193–212, 1984.
- F. Draxler, S. Wahl, C. Schnörr, and U. Köthe. On the universality of volume-preserving and coupling-based normalizing flows. In *Proceedings of the 41st International Conference on Machine Learning*, pages 11613–11641, 2024.
- T. Geffner, G. Papamakarios, and A. Mnih. Compositional score modeling for simulation-based inference. In *International Conference on Machine Learning*, pages 11098–11116. PMLR, 2023.
- A. Gelman, J. B. Carlin, H. S. Stern, D. B. Dunson, A. Vehtari, and D. B. Rubin. *Bayesian Data Analysis (3rd Edition)*. Chapman and Hall/CRC, 2013.
- A. Gelman, A. Vehtari, D. Simpson, C. C. Margossian, B. Carpenter, Y. Yao, L. Kennedy, J. Gabry, P.-C. Bürkner, and M. Modrák. Bayesian workflow. *arXiv preprint arXiv:2011.01808*, 2020.
- M. Gloeckler, M. Deistler, C. Weilbach, F. Wood, and J. H. Macke. All-in-one simulation-based inference. In *Proceedings of the 41st International Conference on Machine Learning*, pages 15735–15766, 2024a.
- M. Gloeckler, S. Toyota, K. Fukumizu, and J. H. Macke. Compositional simulation-based inference for time series. *arXiv preprint arXiv:2411.02728*, 2024b.
- T. Gneiting, F. Balabdaoui, and A. E. Raftery. Probabilistic Forecasts, Calibration and Sharpness. *Journal of the Royal Statistical Society Series B: Statistical Methodology*, 69(2):243–268, 2007. doi: 10.1111/j.1467-9868.2007.00587.x.
- D. Habermann, M. Schmitt, L. Kühmichel, A. Bulling, S. T. Radev, and P.-C. Bürkner. Amortized bayesian multilevel models. *arXiv preprint arXiv:2408.13230*, 2024.
- L. Heinrich, S. Mishra-Sharma, C. Pollard, and P. Windischhofer. Hierarchical neural simulation-based inference over event ensembles. *arXiv preprint arXiv:2306.12584*, 2023.
- J. Ho, A. Jain, and P. Abbeel. Denoising diffusion probabilistic models. *Advances in neural information processing systems*, 33:6840–6851, 2020.
- M. D. Hoffman, A. Gelman, et al. The no-u-turn sampler: adaptively setting path lengths in hamiltonian monte carlo. *J. Mach. Learn. Res.*, 15(1):1593–1623, 2014.
- A. Jolicoeur-Martineau, K. Li, R. Piché-Taillefer, T. Kachman, and I. Mitliagkas. Gotta go fast when generating data with score-based models. *arXiv preprint arXiv:2105.14080*, 2021.
- T. Karras, M. Aittala, T. Aila, and S. Laine. Elucidating the design space of diffusion-based generative models. *Advances in neural information processing systems*, 35:26565–26577, 2022.
- D. Kingma and R. Gao. Understanding diffusion objectives as the elbo with simple data augmentation. *Advances in Neural Information Processing Systems*, 36:65484–65516, 2023.
- Z. Li, H. Yuan, K. Huang, C. Ni, Y. Ye, M. Chen, and M. Wang. Diffusion model for data-driven black-box optimization. *arXiv preprint arXiv:2403.13219*, 2024.
- J. Linhart, G. V. Cardoso, A. Gramfort, S. L. Corff, and P. L. Rodrigues. Diffusion posterior sampling for simulation-based inference in tall data settings. *arXiv preprint arXiv:2404.07593*, 2024.

- J.-M. Lueckmann, J. Boelts, D. Greenberg, P. Goncalves, and J. Macke. Benchmarking simulation-based inference. In *International conference on artificial intelligence and statistics*, pages 343–351. PMLR, 2021.
- C. C. Margossian and L. K. Saul. The shrinkage-delinkage trade-off: An analysis of factorized gaussian approximations for variational inference. In *Uncertainty in Artificial Intelligence*, pages 1358–1367. PMLR, 2023.
- R. McElreath. *Statistical rethinking: A Bayesian course with examples in R and Stan*. Chapman and Hall/CRC, 2018.
- A. Q. Nichol and P. Dhariwal. Improved denoising diffusion probabilistic models. In *International conference on machine learning*, pages 8162–8171. PMLR, 2021.
- V. Pandey, I. Erbas, X. Michalet, A. Ulku, C. Bruschini, E. Charbon, M. Barroso, and X. Intes. Deep learning-based temporal deconvolution for photon time-of-flight distribution retrieval. *Optics letters*, 49(22):6457–6460, 2024.
- V. Pandey, E. Millar, I. Erbas, L. M. Chavez, J. Radford, I. Crosbourne, M. Madhusudan, G. G. Taylor, N. Yuan, C. Bruschini, et al. Real-time wide-field fluorescence lifetime imaging via single-snapshot acquisition for biomedical applications. *bioRxiv*, pages 2025–04, 2025.
- X. Peng, L. Li, and F.-Y. Wang. Accelerating minibatch stochastic gradient descent using typicality sampling. *IEEE transactions on neural networks and learning systems*, 31(11):4649–4659, 2019.
- S. T. Radev, U. K. Mertens, A. Voss, L. Ardizzone, and U. Kothe. Bayesflow: Learning complex stochastic models with invertible neural networks. *IEEE Transactions on Neural Networks and Learning Systems*, 33(4):1452–1466, Apr. 2020. ISSN 2162-2388. doi: 10.1109/tnnls.2020.3042395.
- P. L. C. Rodrigues, T. Moreau, G. Louppe, and A. Gramfort. Hnpe: Leveraging global parameters for neural posterior estimation, 2021.
- M. I. Rowley, A. C. Coolen, B. Vojnovic, and P. R. Barber. Robust bayesian fluorescence lifetime estimation, decay model selection and instrument response determination for low-intensity flim imaging. *PLoS one*, 11(6):e0158404, 2016.
- T. Säilynoja, P.-C. Bürkner, and A. Vehtari. Graphical test for discrete uniformity and its applications in goodness-of-fit evaluation and multiple sample comparison. *Statistics and Computing*, 32(2):32, 2022.
- T. Salimans and J. Ho. Progressive distillation for fast sampling of diffusion models. *arXiv preprint arXiv:2202.00512*, 2022.
- L. Sharrock, J. Simons, S. Liu, and M. Beaumont. Sequential neural score estimation: Likelihood-free inference with conditional score based diffusion models. In *International Conference on Machine Learning*, pages 44565–44602. PMLR, 2024.
- S. A. Sisson and Y. Fan. Likelihood-free mcmc. *Handbook of Markov Chain Monte Carlo*, pages 313–335, 2011.
- J. T. Smith, R. Yao, N. Sinsuebphon, A. Rudkouskaya, N. Un, J. Mazurkiewicz, M. Barroso, P. Yan, and X. Intes. Fast fit-free analysis of fluorescence lifetime imaging via deep learning. *Proceedings of the national academy of sciences*, 116(48):24019–24030, 2019.
- Y. Song and S. Ermon. Generative modeling by estimating gradients of the data distribution. *Advances in neural information processing systems*, 32, 2019.
- Y. Song, J. Sohl-Dickstein, D. P. Kingma, A. Kumar, S. Ermon, and B. Poole. Score-based generative modeling through stochastic differential equations. *arXiv preprint arXiv:2011.13456*, 2020.
- Y. Song, C. Durkan, I. Murray, and S. Ermon. Maximum likelihood training of score-based diffusion models. *Advances in neural information processing systems*, 34:1415–1428, 2021.

- N. Tolley, P. L. Rodrigues, A. Gramfort, and S. R. Jones. Methods and considerations for estimating parameters in biophysically detailed neural models with simulation based inference. *PLOS Computational Biology*, 20(2):e1011108, 2024.
- B. Torrado, B. Pannunzio, L. Malacrida, and M. A. Digman. Fluorescence lifetime imaging microscopy. *Nature Reviews Methods Primers*, 4(1):80, 2024.
- A. L. Trinh and A. Esposito. Biochemical resolving power of fluorescence lifetime imaging: untangling the roles of the instrument response function and photon-statistics. *Biomedical optics express*, 12(7):3775–3788, 2021.
- A. Verma, V. Pandey, C. Sherry, T. Humphrey, C. James, K. Matteson, J. T. Smith, A. Rudkouskaya, X. Intes, and M. Barroso. Fluorescence lifetime imaging for quantification of targeted drug delivery in varying tumor microenvironments. *Advanced Science*, 12(3):2403253, 2025.
- S. Wang, J. V. Chacko, A. K. Sagar, K. W. Eliceiri, and M. Yuan. Nonparametric empirical bayesian framework for fluorescence-lifetime imaging microscopy. *Biomedical optics express*, 10(11):5497–5517, 2019.
- N. Yuan, V. Pandey, A. Verma, T. Humphrey, M. Barroso, X. Intes, and X. Michalet. Quantifying lifetime uncertainty in gated-iccd fluorescence lifetime imaging. 2024.
- M. Zaheer, S. Kottur, S. Ravanbakhsh, B. Poczos, R. R. Salakhutdinov, and A. J. Smola. Deep sets. *Advances in neural information processing systems*, 30, 2017.
- Y. Zhang and L. Mikelsons. Solving stochastic inverse problems with stochastic bayesflow. In *2023 IEEE/ASME International Conference on Advanced Intelligent Mechatronics (AIM)*, pages 966–972, 2023. doi: 10.1109/AIM46323.2023.10196190.

A Appendix

A.1 Stochastic differential equation formulation of the diffusion process

The forward diffusion process for $t \in [0, 1]$ can be specified as a stochastic differential equation Song et al. [2020]:

$$d\boldsymbol{\theta}_t = f(\boldsymbol{\theta}_t, t) dt + g(t) d\mathbf{W}_t.$$

For a known variance-preserving process, the drift and diffusion coefficients are given by

$$f(\boldsymbol{\theta}, t) = -\frac{1}{2} \left(\frac{d}{dt} \log(1 + e^{-\lambda_t}) \right) \boldsymbol{\theta}, \quad g(t)^2 = \frac{d}{dt} \log(1 + e^{-\lambda_t}),$$

with $\alpha_t^2 = \text{sigmoid}(\lambda_t)$ and $\sigma_t^2 = \text{sigmoid}(-\lambda_t)$ as discussed in [Kingma and Gao, 2023]. Time can be reversed via the reverse-time SDE

$$d\boldsymbol{\theta}_t = [f(\boldsymbol{\theta}_t, t) - g(t)^2 \nabla_{\boldsymbol{\theta}_t} \log p_t(\boldsymbol{\theta}_t | \mathbf{Y})] dt + g(t) d\mathbf{W}_t,$$

which enables posterior sampling using state-of-the-art SDE solvers. The corresponding probability ODE is

$$d\boldsymbol{\theta}_t = \left[f(\boldsymbol{\theta}_t, t) - \frac{1}{2} g(t)^2 \nabla_{\boldsymbol{\theta}_t} \log p_t(\boldsymbol{\theta}_t | \mathbf{Y}) \right] dt.$$

A.2 Mini-batch estimator is unbiased

Proposition 2. *The mini-batch estimator*

$$\hat{s}_\psi(\boldsymbol{\theta}, \mathbf{Y}, \lambda_t) = (1 - J)(1 - t) \nabla_{\boldsymbol{\theta}} \log p(\boldsymbol{\theta}) + \frac{J}{M} \sum_{j=1}^M s_\psi(\boldsymbol{\theta}, \mathbf{Y}_j, \lambda_t)$$

with M samples, where each sample \mathbf{Y}_j is sampled uniformly from the set $\{\mathbf{Y}_1, \dots, \mathbf{Y}_J\}$, is an unbiased estimator of the full compositional score.

Proof. By linearity of expectation, we have

$$\mathbb{E} \left[\frac{J}{M} \sum_{j=1}^M s_\psi(\boldsymbol{\theta}, \mathbf{Y}_j, \lambda_t) \right] = \frac{J}{M} \sum_{j=1}^M \mathbb{E}_{\mathbf{Y}_j} [s_\psi(\boldsymbol{\theta}, \mathbf{Y}_j, \lambda_t)].$$

Since each \mathbf{Y}_j is sampled uniformly from $\{\mathbf{Y}_1, \dots, \mathbf{Y}_J\}$,

$$\mathbb{E}_{\mathbf{Y}_j} [s_\psi(\boldsymbol{\theta}, \mathbf{Y}_j, \lambda_t)] = \frac{1}{J} \sum_{j=1}^J s_\psi(\boldsymbol{\theta}, \mathbf{Y}_j, \lambda_t),$$

so

$$\mathbb{E} \left[\frac{J}{M} \sum_{j=1}^M s_\psi(\boldsymbol{\theta}, \mathbf{Y}_j, \lambda_t) \right] = \frac{J}{M} \cdot M \cdot \frac{1}{J} \sum_{j=1}^J s_\psi(\boldsymbol{\theta}, \mathbf{Y}_j, \lambda_t) = \sum_{j=1}^J s_\psi(\boldsymbol{\theta}, \mathbf{Y}_j, \lambda_t).$$

Adding the constant prior term $(1 - J)(1 - t) \nabla_{\boldsymbol{\theta}} \log p(\boldsymbol{\theta})$ yields the full compositional score. Hence, the estimator is unbiased. \square

A.3 Evaluation metrics

All experiments are repeated 10 times and the median and median absolute deviation from the following standard metrics are reported:

Root mean squared error (RMSE). RMSE measures the deviation between posterior samples and the ground-truth parameters. Given posterior samples $\hat{\boldsymbol{\theta}}_{ij}^{(s)}$ for parameters j in dataset i , and true parameters $\boldsymbol{\theta}_{ij}$, the RMSE is defined as:

$$\text{RMSE}_j = \sqrt{\frac{1}{S} \sum_{s=1}^S \left(\hat{\boldsymbol{\theta}}_{ij}^{(s)} - \boldsymbol{\theta}_{ij} \right)^2},$$

aggregated over datasets via median and over the parameters j via the mean. We normalize RMSE by dividing by the empirical range of the ground-truth parameters.

Calibration error. Calibration Error measures how well the empirical coverage of posterior credible intervals matches their nominal level. For a level $\alpha \in [0.005, 0.995]$, we compute the α -credible interval for each parameter and check whether the ground-truth value falls within it. Let I_{ij}^α denote the indicator that the true value lies within the interval:

$$\text{CalibrationError}_j = \text{median}_\alpha \left| \frac{1}{N} \sum_{i=1}^N I_{ij}^\alpha - \alpha \right|,$$

where aggregation is across a grid of α values. We calculate the mean calibration error over the parameters j . This metric is sensitive to both over- and under-confidence in the posteriors.

Posterior contraction. We define posterior contraction as the relative reduction in variance from prior to posterior:

$$\text{Contraction}_j = 1 - \frac{\text{Var}_{\text{posterior}}(\theta_j)}{\text{Var}_{\text{prior}}(\theta_j)},$$

where values are clipped to $[0, 1]$. This reflects how much uncertainty has been reduced due to conditioning on the data, with values near 1 indicating strong learning.

KL divergence (Gaussian case). In the Gaussian toy example, where the true posterior is analytically tractable and Gaussian, we compute the KL divergence between the empirical posterior $q(\theta)$ (estimated from samples) and the true Gaussian posterior $p(\theta)$:

$$\text{KL}(q \| p) = \frac{1}{2} \left[\log \frac{|\Sigma_p|}{|\Sigma_q|} - d + \text{Tr}(\Sigma_p^{-1} \Sigma_q) + (\mu_q - \mu_p)^\top \Sigma_p^{-1} (\mu_q - \mu_p) \right],$$

where μ_q, Σ_q are the empirical mean and covariance of posterior samples, and μ_p, Σ_p are the parameters of the analytical posterior.

A.4 Score model architectures & training

- **MLPs:** Fully connected networks with 5 hidden layers and 256 units per layer, using Mish activations.
- **Residual local conditioning:** Local networks receive a projection of the global latent variables and learn a residual update. Otherwise, global and local network are simple MLPs.
- **Permutation-invariant aggregation:** To handle multiple condition sets or observations per group, we use a shallow permutation-invariant encoder architecture based on the Deep Set framework Zaheer et al. [2017]:
 - An encoder MLP (enc) with 4 layers of 128 hidden units and ReLU activations,
 - Mean pooling over the set dimension to ensure permutation invariance,
 - A decoder MLP (dec) with 3 hidden layers (each of size 128) and ReLU activations, projecting to the final output dimension.
- **Time series summary network:** For structured input data such as time series (as in the FLI application), we use a hybrid convolutional–recurrent architecture. The model begins with a stack of 1D convolutional layers followed by a skipping recurrent path as implemented in [Zhang and Mikelsons, 2023]:
 - A standard recurrent path (bidirectional GRU with hidden size 256),
 - A skip-convolution path, which downsamples the sequence via strided convolution and feeds the result into a parallel recurrent layer,
 - Final representations from both paths are concatenated to produce a summary embedding which are then projected by a linear layer to a fixed summary dimension of size 18.

We parameterize our score models to predict the more stable $\hat{\mathbf{v}}_t := \alpha_t \epsilon - \sigma_t \theta_t$, and then transform the output to $\hat{\epsilon}_t$, as it has been shown that this parameterization is more stable for all t , whereas noise-prediction becomes harder for t close to 0 where the signal increases and noise decreases Salimans and Ho [2022]. Furthermore, we condition the score network on the signal-to-noise ratio (SNR), normalized to the interval $[-1, 1]$ similar to the preconditioning introduced in [Karras et al., 2022]. The data and parameters are always standardized, and the prior scores are adjusted accordingly by multiplying them by the standard deviation of the parameters.

Noise schedules We employed the following schedules:

- **Cosine schedule** by Nichol and Dhariwal [2021] (with $s=0$ during training)

$$\lambda(t) = -2 \log(\tan(\pi t/2)) + 2s,$$

- **Linear schedule** by Ho et al. [2020]

$$\lambda(t) = -\log(e^{t^2} - 1),$$

- and **EDM schedule** by Karras et al. [2022] for training

$$\lambda(t) = \mathcal{F}_{\mathcal{N}}^{-1}(t; 2.4, 2.4^2)$$

and sampling

$$\lambda(t) = -2\rho \log(\sigma_{\max}^{1/\rho} + (1-t)(\sigma_{\min}^{1/\rho} - \sigma_{\max}^{1/\rho}))$$

with $\rho = 7$, $\sigma_{\min} = 0.002$, $\sigma_{\max} = 80$, and $\sigma_{\text{data}} = 1$.

All our noise schedules are truncated such that the log signal-to-noise ratio is $\lambda_t \in [-15, 15]$ to avoid instabilities in sampling as detailed in [Kingma and Gao, 2023]. For the EDM schedule we set $\lambda_t \in [-\log \sigma_{\max}^2, -\log \sigma_{\min}^2]$ as in the original paper.

As weighting function for the loss, we employed the likelihood weighting $w_t = g(t)^2/\sigma^2$ proposed by Song et al. [2021] for the linear and cosine schedules and the original EDM weighting $w_t = \exp(-\lambda_t) + 1$ for the EDM schedule [Karras et al., 2022].

Training We trained all models using AdamW with a cosine annealing learning rate schedule. The initial learning rate is set to 5×10^{-4} . Models are trained for 1000 epochs on the Gaussian toy example and 3000 epochs on all other settings. In each epoch we generate 10,000 new training samples on the fly. Only for the FLI application we used 30,000 samples per epoch as we found that more training data was needed.

All models were trained on a high-performance computing cluster using a AMD EPYC "Milan" CPU (2.00 GHz), 100 GB DDR4 3200 MHz RAM, and a NVIDIA A40 GPU with 48 GB of memory. Each experiment required 1-2 days for all repeated runs on a high-performance computing infrastructure with up to 50 parallel jobs.

Sampling For our experiments, we used the adaptive second-order sampler with maximal 10,000 iterations and the default settings proposed by Jolicœur-Martineau et al. [2021]. Specifically, we set the absolute error tolerance to $e_{\text{abs}} = 0.01 \times \text{the number of parameters}$ and the relative tolerance to $e_{\text{rel}} = 0.5$. To solve the probability ODE, we used an Euler scheme. For annealed Langevin dynamics, we followed the setup from Geffner et al. [2023], using 5 Langevin steps per iteration, a maximum of 2000 iterations, and a step size factor of 0.1.

To find the optimal damping factor d_1 and optimal shift s for a certain task, we run a hyper-parameter search optimizing the combined loss of RMSE and calibration error on a test data set. We also considered $d_0 < 1$, and found that sometimes this can improve accuracy of the posterior, even though the true posterior is theoretically not recovered.

Code The software code and data for the experiments is available in a public GitHub repository: <https://anonymous.4open.science/r/hierarchical-abi-submission-7409/>.

A.5 Experiment 1: Gaussian toy model

Model definition:

$$\theta \sim \mathcal{N}(\theta, \sigma \mathbf{I})$$

with $\sigma = 0.1$ and dimension set to 10. Given a normal prior, with the same scale, the posterior is also Gaussian and we can calculate it analytically. Here, we do not employ a summary network.

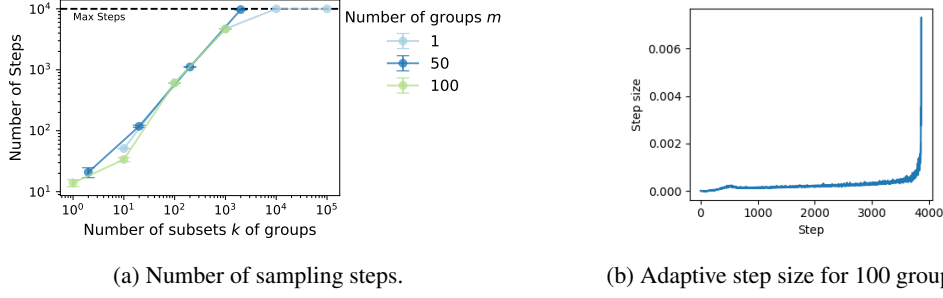


Figure 6: *Assessing the adaptive sampling scheme for compositional inference in the toy model.* (a) Increasing numbers of sampling steps are needed for increasing number of subsets of groups. (b) The adaptive step size is adaptively increased towards the end of the sampling (low noise region).

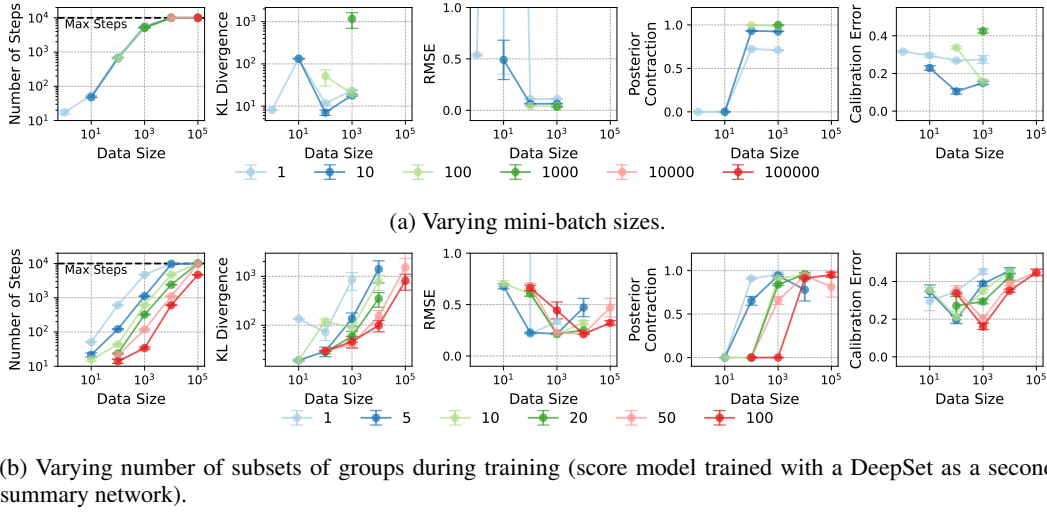


Figure 7: *Evaluation of the error-damping estimator for the toy model.* Different evaluation metrics are shown for different mini-batch sizes or varying numbers of subsets of groups. For each experiment 10 runs were performed. The median and median absolute deviation is reported besides for those runs where none converged.

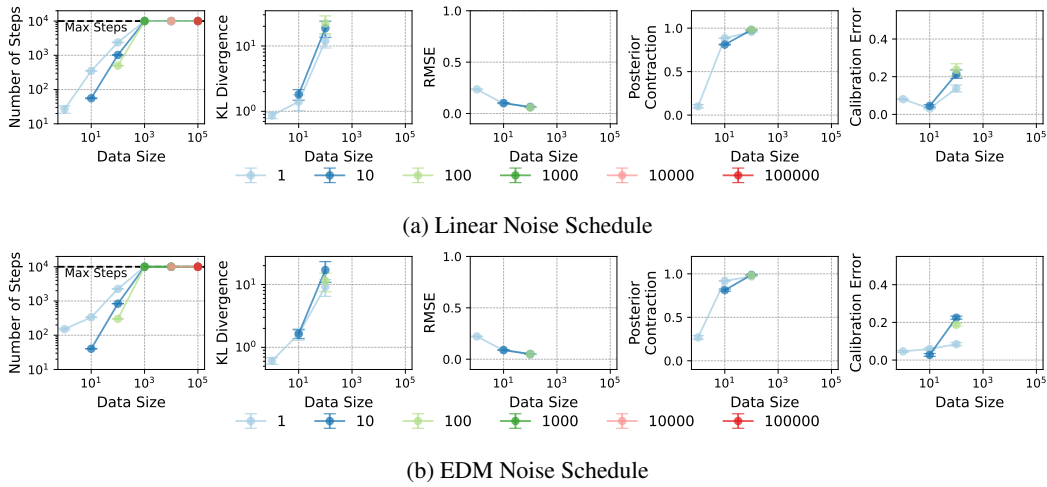


Figure 8: *Evaluation of the different noise schedules for the toy model.* For each experiment 10 runs were performed. The median and median absolute deviation is reported besides for those runs where none converged. Both methods fail for already 1,000 groups, where the standard cosine schedule still converges.

A.6 Experiment 2: hierarchical AR(1) model

Our hyper-priors are defined as follows:

$$\alpha \sim \mathcal{N}(0, 1), \quad \beta \sim \mathcal{N}(0, 1), \quad \log \sigma \sim \mathcal{N}(0, 1).$$

The local parameters are different for each grid point:

$$\tilde{\eta}_j \sim \mathcal{N}(0, \sigma \mathbf{I}), \quad \eta_j = 2 \text{sigmoid}(\beta + \tilde{\eta}_j) - 1.$$

In each grid point j , we have a time series of $T = 5$ observations,

$$\begin{aligned} \mathbf{Y}_{j,0} &\sim \mathcal{N}(0, 0.1\mathbf{I}) \\ \mathbf{Y}_{j,t} &\sim \mathcal{N}(\alpha + \eta_j \mathbf{Y}_{j,t-1}, 0.1\mathbf{I}), \quad t = 1, \dots, T-1. \end{aligned}$$

On the local level, we perform inference on $\tilde{\eta}$ and afterwards transform $\tilde{\eta}$ to η as NUTS [as implemented in Stan Carpenter et al., 2017] performs better on non-centered parameterizations [Betancourt and Girolami, 2015]. Here, we do not employ a summary network.

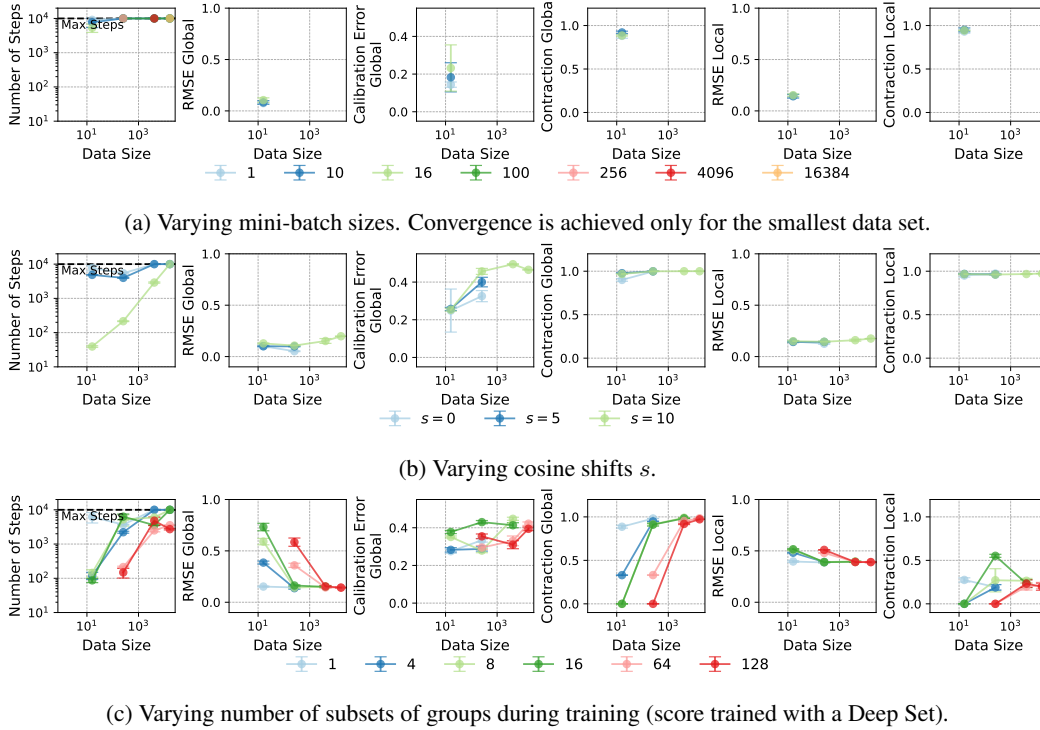


Figure 9: *Evaluation of the error-damping estimator for the hierarchical AR(1) model.* For each experiment 10 runs were performed. The median and median absolute deviation is reported besides for those runs where none converged. A mini-batch size of 10% of the data is employed and score models are trained on a single group.

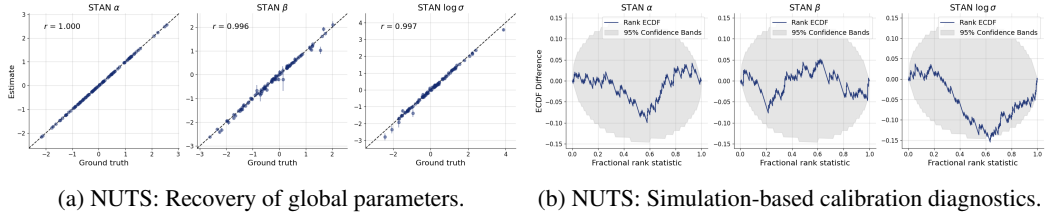


Figure 10: *Calibration verification of NUTS*. NUTS, regarded as a gold standard for Bayesian inference, can recover global parameters and is well calibrated for the 32×32 grid. However, for larger grids the computational costs explode.

A.7 Experiment 3: fluorescence lifetime imaging (FLI) model

Model The observed time-resolved fluorescence signal at each pixel is modeled using a bi-exponential function, following the work of Pandey et al. [2024] and Smith et al. [2019]. This approach captures the fluorescence decay dynamics of individual fluorophores, accounting for both fast and slow decay components associated with different molecular states. By fitting a decay model, we can extract information about the characteristic lifetimes of the fluorophores, which is essential for studying molecular interactions and dynamics. The time-dependent fluorescence signal is given as:

$$y(t) = I \cdot \left[A^L e^{-t/\tau_1^L} + (1 - A^L) e^{-t/\tau_2^L} \right] * \text{IRF}(t) + \eta(t), \quad (12)$$

where τ_1^L, τ_2^L are the fluorescence lifetimes and A^L is a mixture parameter. Here, $I \in [0, 1024]$ denotes the pixel intensity for 10-bit images, $\text{IRF}(t)$ is the instrument response function, and $\eta(t)$ represents additive noise. The symbol $*$ denotes convolution. For each simulation, we independently sample a time series from the recorded IRF and system generated noise. The maximal photon count in each time series is then normalized to 1. The real data is also normalized to 1 on a pixel-wise level.

Instrument response function (IRF) The emitted signals are recorded using multiple instruments (detectors, electronics, etc.) which have a characteristic response $E(t)$ to an instantaneous signal $\delta(t)$ (e.g., a single photon). The recorded signals from the T -periodic emitted signal can be written as a convolution of periodic $\delta_{0,T}$ and non-periodic $E(t)$:

$$\begin{aligned} y_0(t) &= E(t) * \delta_{0,T}(t) \\ &= E(t) * (x_{0,T} * F_{0,T}) \\ &= (E(t) * x_{0,T}) * F_{0,T} \\ &= \text{IRF}_{0,T} * F_{0,T}. \end{aligned} \quad (13)$$

Equation 13 introduces the T -periodic instrument response function $\text{IRF}_{0,T}$. The IRF can be measured using excitation signal from diffused white paper. The FLI experimental details in microscopy, mesoscopy and macrosopy can be found in Pandey et al. [2025].

The traditional ways of fitting this kind of models are reviewed in Torrado et al. [2024].

Priors The prior distributions were designed with domain knowledge:

$$\begin{aligned} \tau_{1,\text{mean}}^G &\sim \mathcal{N}(\log(0.2), 0.7^2), & \tau_{1,\text{std}}^G &\sim \mathcal{N}(-1, 0.1^2), \\ \Delta\tau_{\text{mean}}^G &\sim \mathcal{N}(\log(1), 0.5^2), & \Delta\tau_{\text{std}}^G &\sim \mathcal{N}(-2, 0.1^2), \\ a_{\text{mean}}^G &\sim \mathcal{N}(0.4, 1^2), & a_{\text{std}}^G &\sim \mathcal{N}(-1, 0.5^2). \end{aligned}$$

Local parameters are then sampled from the corresponding global means and standard deviations:

$$\tau_{1,j}^L \sim \mathcal{N}(\tau_{1,\text{mean}}^G, (\tau_{1,\text{std}}^G)^2), \quad \Delta\tau_j^L \sim \mathcal{N}(\Delta\tau_{\text{mean}}^G, (\Delta\tau_{\text{std}}^G)^2), \quad a_j^L \sim \mathcal{N}(a_{\text{mean}}^G, (a_{\text{std}}^G)^2).$$

The local parameters can then be converted to linear scale for simulation:

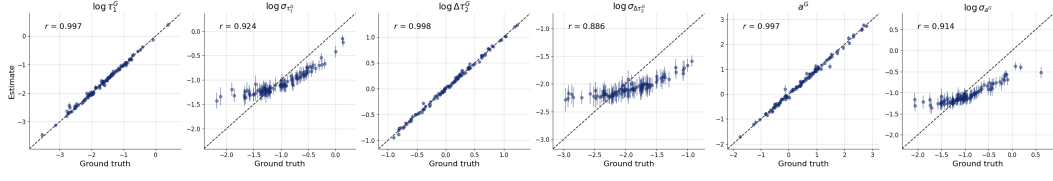
$$\tau_1^L = \exp(\log \tau_1), \quad \tau_2^L = \tau + \exp(\log \Delta\tau), \quad A^L = \frac{1}{1 + \exp(-a)}.$$

This ensures that $\tau_2 > \tau_1$ on both global and local levels and that the mixture fulfills $A \in [0, 1]$. Additionally, we can compute the average lifetime $\tau_{\text{mean}} = A\tau_1 + (1 - A)\tau_2$.

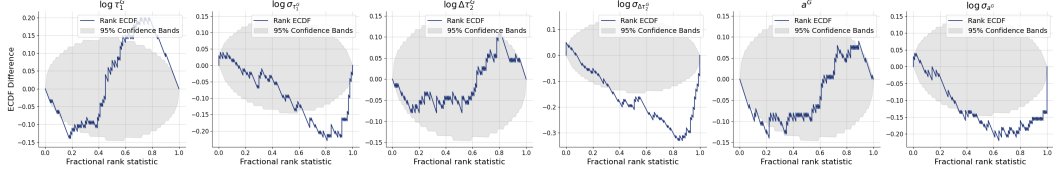
Alternatively, we could have used a non-centered parameterization commonly found in the mixed-effects literature (such as for the hierarchical AR(1) model), where global means are treated as fixed effects and local parameters as additive random effects with a mean of zero and the same standard deviation as described above.

Here, we employ the time series summary network.

Data AU565 (HER2+ human breast carcinoma) cells, incubated for 24h with 20 $\mu\text{g/mL}$ TzM-Alexa Fluor 700 (Donor, D) and 40 $\mu\text{g/mL}$ TzM-Alexa Fluor 750 (Acceptor, A), were imaged using Förster resonance energy transfer (FRET) microscopy to quantify trastuzumab (TzM) binding. AU565 cells exhibit relative low level of HER2 heterodimerization that correlate with reduced TzM uptake and sensitivity, which is also influenced by culture conditions (2D vs 3D). FLI-FRET analysis allows for the quantification of these dimerization-dependent variations in live cells by assessing the proximity of donor and acceptor-labeled TzM.

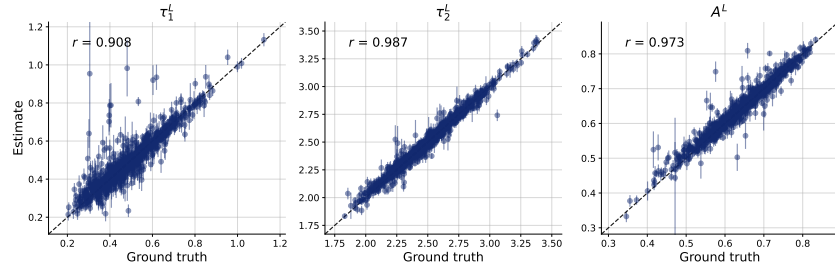


(a) Recovery of global parameters with hierarchical score based approach (medians and median absolute deviation of the posterior samples).

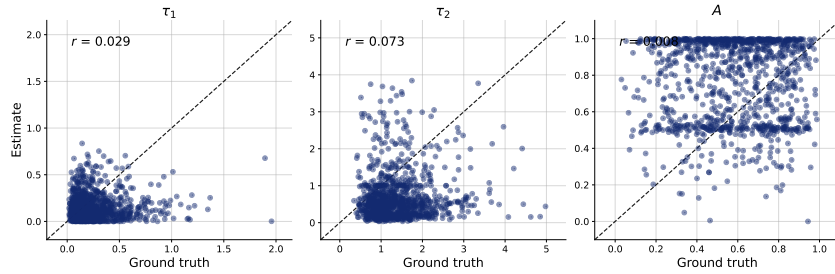


(b) Global posterior calibration assessed with simulation-based calibration diagnostics.

Figure 11: Assessing inference of global parameters for the FLI model. Synthetic data on a 32×32 grid was generated.

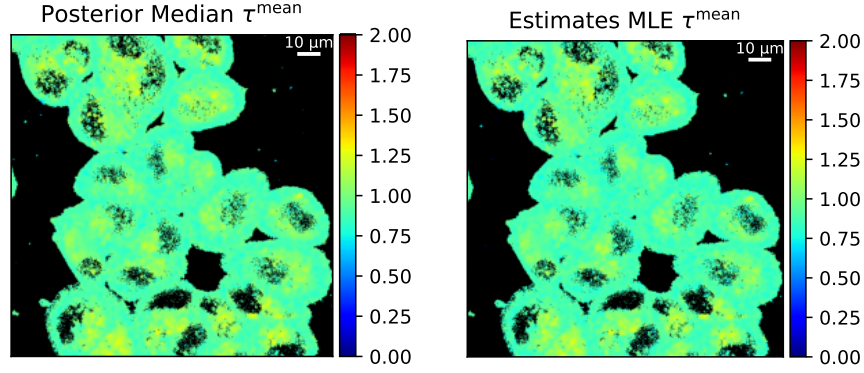


(a) Recovery of transformed local parameters for one 32×32 grid with hierarchical score based approach (medians and median absolute deviation of the posterior samples). Deviations from the ground truth can be due to the expected shrinkage of the local posteriors.



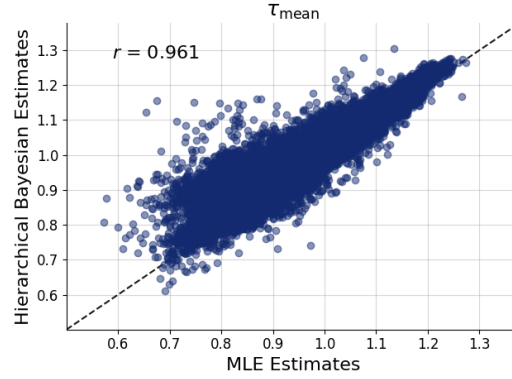
(b) Recovery of transformed local parameters with MLE.

Figure 12: Assessing inference of local parameters for the FLI model. Synthetic data on a 32×32 grid was generated. We compare our hierarchical approach against the standard non-hierarchical pixel-wise MLE.



(a) Hierarchical τ_{mean} estimates.

(b) MLE τ_{mean} estimates.



(c) Correlation of τ_{mean} estimates. Our local posterior medians vs. pixel-wise MLE estimates.

Figure 13: *Assessing inference of local parameters for the FLI model on real data.* We compare our hierarchical approach against the standard non-hierarchical pixel-wise MLE. Due to low photon count, the average lifetime τ^{mean} is the most reliable quantity for this non-hierarchical method.

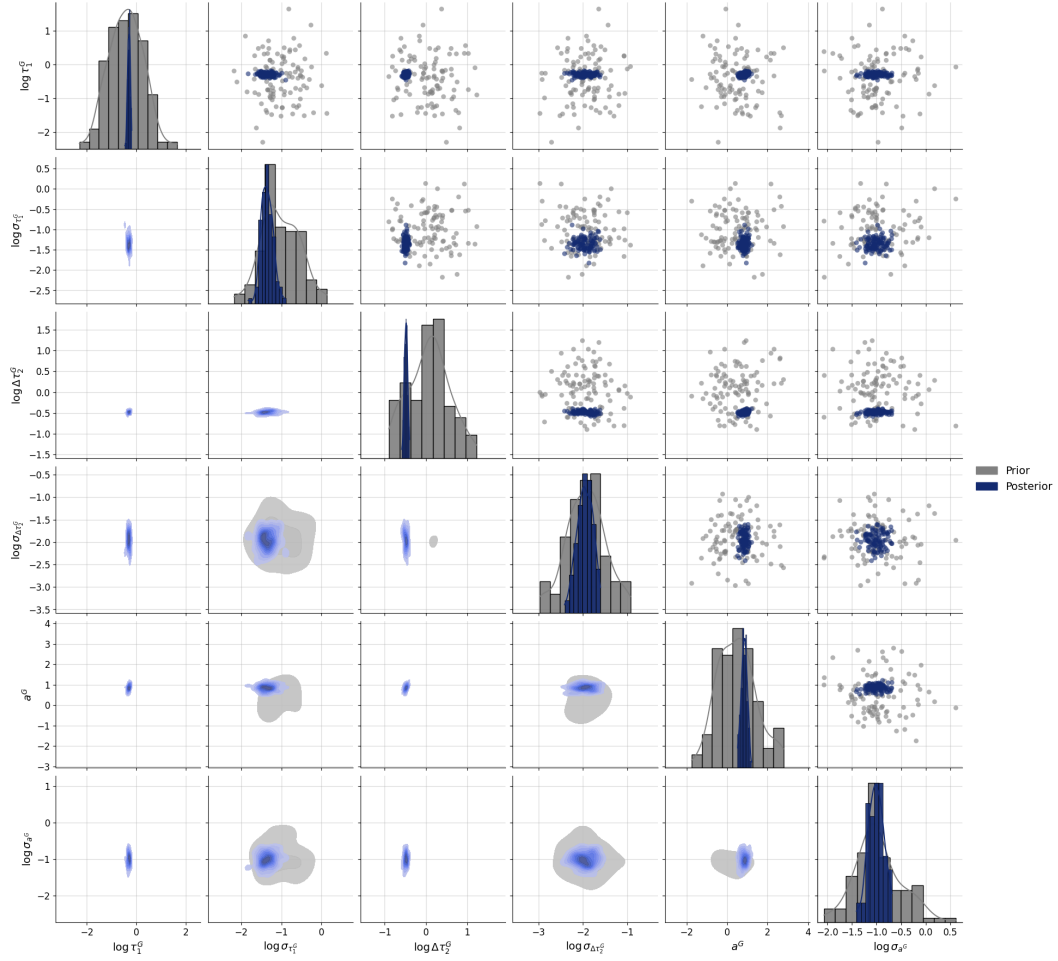


Figure 14: Global posteriors for the real FLI data.